STRUCTURAL BIOLOGY COMMUNICATIONS

ISSN 2053-230X

Production, crystallization and structure determination of a mycobacterial glucosylglycerate hydrolase

Tatiana Barros Cereija,[a,b,c] Susana Alarico,[d,e] Nuno Empadinhas[d,e] and Pedro José Barbosa Pereira[a,b]*

[a]Biomolecular Structure and Function, IBMC – Instituto de Biologia Molecular e Celular, Universidade do Porto, Porto, Portugal, [b]I3S – Instituto de Investigação e Inovação em Saúde, Universidade do Porto, Porto, Portugal, [c]ICBAS – Instituto de Ciências Biomédicas Abel Salazar, Porto, Portugal, [d]Molecular Mycobacteriology and Microbiome, CNC – Centro de Neurociências e Biologia Celular, Universidade de Coimbra, Coimbra, Portugal, and [e]III/UC – Instituto de Investigação Interdisciplinar, Universidade de Coimbra, Coimbra, Portugal. *Correspondence e-mail: ppereira@ibmc.up.pt

Received 26 June 2017
Accepted 28 August 2017

Edited by R. Sankaranarayanan, Centre for Cellular and Molecular Biology, Hyderabad, India

Keywords: *Mycobacterium hassiacum*; GH63; glucosylglycerate hydrolase; nitrogen starvation; multiwavelength anomalous diffraction.

Glucosylglycerate hydrolase is highly conserved among rapidly growing mycobacteria and has been found to be involved in recovery from nitrogen starvation by promoting the rapid mobilization of the glucosylglycerate that accumulates under these conditions. Here, the production, crystallization and structure determination of glucosylglycerate hydrolase from *Mycobacterium hassiacum* using two-wavelength anomalous diffraction of selenomethionine-substituted crystals are described. The monoclinic (space group $P2_1$) crystals diffracted to ~2.0 Å resolution at a synchrotron-radiation source and contained four molecules in the asymmetric unit, corresponding to a Matthews coefficient of 3.07 Å^3 Da^{-1} and a solvent content of 59.9%. The quality of the experimental phases allowed the automated building of 1677 of the 1792 residues in the asymmetric unit.

1. Introduction

Nontuberculous mycobacteria (NTM), which include species other than the *Mycobacterium tuberculosis* complex and *M. leprae*, are receiving increasing attention. Many of these ubiquitous environmental bacteria are opportunistic pathogens that are capable of causing lymphadenopathy in children, pulmonary, skin and soft-tissue infections or even disseminated infections, particularly in susceptible individuals (Griffith *et al.*, 2007; Piersimoni & Scarparo, 2008; Henkle & Winthrop, 2015). Since NTM are exposed to several environmental challenges, they display high resilience against stress conditions, including nutrient starvation, desiccation, pH and temperature variations, as well as antibiotic and disinfectant action (Falkinham, 2010). These characteristics allow them to colonize artificial environments such as domestic and hospital water-distribution systems, from where they easily access susceptible hosts. Moreover, NTM are naturally resistant to common antibiotics and some infections do not even respond to aggressive antitubercular treatments (Shahraki *et al.*, 2015; Griffith *et al.*, 2015; Nunes-Costa *et al.*, 2016). NTM infections are thus becoming a considerable clinical challenge for which therapeutic solutions are scarce. No significant treatment advances for NTM infection in general have recently been accomplished and the increasing resistance of some mycobacterial species to the therapeutics currently in use reinforces the need for more active drug development (Nessar *et al.*, 2012).

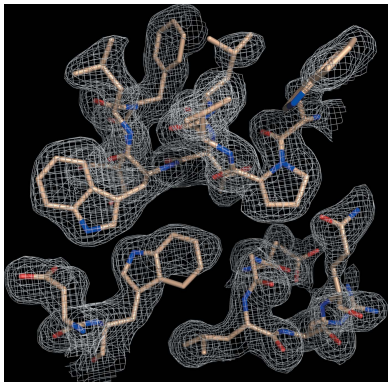

Table 1
Macromolecule-production information.

Source organism	*M. hassiacum* DSM 44199T (Tiago *et al.*, 2012)
DNA source	pET-30a-*Mh*GgH (Alarico *et al.*, 2014)
Forward primer†	TATACGTCTCACATGCCGCACGACCCGAGTTTCAC
Reverse primer‡	CGAATTCTTAGCCCAGCCAGTCGAGCACC
Cloning and expression vector	pETM11
Expression host	*Mh*GgH, *E. coli* BL21 (DE3); SeMet-*Mh*GgH, *E. coli* B834 (DE3)
Complete amino-acid sequence of the construct produced§	*MKHHHHHHPMSDYDIPTTENLYFQ*GAMPHDPSFTPTQLAARAAYLLRGNDLGTMTTAAPLLYPHMWSWDAAFVAIGLAPLSVERAVVELDTLLSAQWRNGMIPHIVFANGVDGYFPGPARWATATLADNAPRNRLTSGITQPPVHAIAVQRILEHARTRGRSTRAVAEAFLDRRWGDLMRWHRWLAECRDRNERGRITLYHGWESGMDNSPRWDSAYANVVPGKLPEYQRADNVIITDPSQRPSDGEYDRYLWLLEEMKAVRYDDERLPSVMSFQVEDVFFSAIFSVACQVLAEIGEDYKRPHADVKDLYLWAERFRAGVVETTDQRTGAARDFDVLAEKWLVTETAAQFAPLLCGGLPHDRERALLKLLEGPRFCGHPDLKYGLIPSTSPVSRDFRPREYWRGPVWPVLTWLFSWCFARRGWAERARLLRQEGLRQASDGSFAEYYEPFTGEPLGSMQQSWTAAAVLDWLG
No. of amino acids	448
Theoretical molecular weight (Da)	50897

† The BsmBI recognition sequence is underlined. ‡ The EcoRI recognition sequence is underlined. § The residues removed by TEV protease cleavage are italicized. The sequence of native *Mh*GgH is underlined.

Glucosylglycerate hydrolase (EC 3.2.1.–) from *M. hassiacum* (*Mh*GgH) catalyses the hydrolysis of glucosylglycerate (GG), which is accumulated during growth with limited nitrogen, into glucose and glycerate (Alarico *et al.*, 2014). Mycobacteria seem to accumulate GG as part of a global response to nitrogen stress, so a mechanism relying on hydrolysis by *Mh*GgH may allow the assimilation of this metabolite when nitrogen availability is restored and thus is likely to contribute to the rapid energy mobilization required for cell growth and division (Behrends *et al.*, 2012; Nunes-Costa *et al.*, 2017). This hydrolase is highly conserved among rapidly growing mycobacteria, reflecting its importance during evolution and its potential as a drug target for the treatment of NTM infections. On the basis of its amino-acid sequence, *Mh*GgH is grouped into glycoside hydrolase family 63 (GH63) and it is likely to adopt the typical $(\alpha/\alpha)_6$ architecture of this family. The GH63 family contains more than 1600 members, including a single enzyme sharing 36% amino-acid sequence identity with *Mh*GgH that has been structurally characterized (Miyazaki *et al.*, 2015). Here, we describe the expression, purification, crystallization and structure determination of *Mh*GgH.

2. Materials and methods

2.1. Macromolecule production

2.1.1. Production of *Mh*GgH. The gene coding for *Mh*GgH was amplified by PCR from a pET-30a-based construct (Alarico *et al.*, 2014) and cloned into the NcoI/EcoRI sites of pETM11, giving the pETM11-*Mh*GgH expression vector (see Table 1 for details). *Escherichia coli* BL21 (DE3) cells transformed with the pETM11-*Mh*GgH plasmid were grown at 301 K in LB medium supplemented with 50 µg ml^{-1} kanamycin to an OD_{600} of 0.7–1.0. At this point, the temperature was decreased to 298 K and expression was induced with 0.5 m*M* isopropyl *β*-D-1-thiogalactopyranoside (IPTG). After overnight growth, the cells were harvested, resuspended in lysis buffer [20 m*M* Tris–HCl pH 8.0, 500 m*M* NaCl, 5 m*M* $MgCl_2$, 1 µg ml^{-1} DNAse, 0.3 mg ml^{-1} lysozyme, 1 m*M* phenylmethylsulfonyl fluoride (PMSF)] and stirred gently on ice for 1 h. The protein extract was clarified by centrifugation, supplemented with 20 m*M* imidazole and loaded onto an immobilized metal-affinity column (Agarose Bead Technologies) loaded with nickel and pre-equilibrated in buffer *A* (20 m*M* Tris–HCl pH 8.0, 500 m*M* NaCl, 20 m*M* imidazole). Bound *Mh*GgH was eluted with 100 m*M* imidazole in buffer *A*. *Mh*GgH-containing fractions were pooled and the His_6 tag was removed by digestion with *Tobacco etch virus* (TEV) protease (1:5 molar ratio) at 277 K concomitantly with overnight dialysis against 20 m*M* Tris–HCl pH 8.0, 500 m*M* NaCl, 0.5 m*M* ethylenediaminetetraacetic acid (EDTA), 1 m*M* dithiothreitol (DTT) (dialysis buffer). Untagged *Mh*GgH was separated from the His_6 tag, tagged *Mh*GgH and TEV protease by a second immobilized metal-affinity chromatography step using the same experimental conditions as described above. The *Mh*GgH-containing column flowthrough was concentrated using a 10 kDa cutoff ultrafiltration device (Millipore) and loaded onto a HiPrep 26/60 Sephacryl S-200 HR size-exclusion column (GE Healthcare) using 20 m*M* Tris–HCl pH 8.0, 400 m*M* NaCl (storage buffer) as the mobile phase. Fractions containing *Mh*GgH were pooled and concentrated using a 10 kDa cutoff ultrafiltration device (Millipore). The concentration of the purified protein was estimated by measuring its absorbance at 280 nm. The purified material was flash-frozen in liquid nitrogen and kept at 193 K until needed. Macromolecule-production information is summarized in Table 1.

2.1.2. Production of selenomethionine-containing *Mh*GgH. *E. coli* B834 (DE3) cells transformed with pETM11-*Mh*GgH were grown in 25 ml LB medium overnight at 310 K. The cells were collected, washed thrice with sterile deionized water and used to inoculate 1 l of SelenoMethionine Medium (Molecular Dimensions). The culture was grown at 303 K to an OD_{600} of 0.7–0.8 before inducing expression with 0.5 m*M* IPTG. After overnight growth, the cells were harvested, resuspended in lysis buffer and incubated on ice with gentle agitation for 1 h. The protein extract was clarified by centrifugation, supplemented with 20 m*M* imidazole and 5 m*M* *β*-mercaptoethanol (*β*-ME), and loaded onto an immobilized metal-affinity column (Agarose Bead Technologies) loaded with nickel and pre-equilibrated with buffer *A* supplemented with 5 m*M* *β*-ME. Bound protein was eluted with 100 m*M* imidazole and 5 m*M* *β*-ME in buffer *A*. Fractions containing selenomethionine-labelled *Mh*GgH (SeMet-*Mh*GgH) were pooled and dialysed in the presence of TEV protease (1:5 molar ratio) against 50 volumes of dialysis buffer containing 400 m*M* NaCl for 2 h at

room temperature followed by overnight incubation at 277 K. Untagged SeMet-*Mh*GgH was separated from the cleaved affinity tag, noncleaved material and TEV protease by a second immobilized-metal affinity chromatography step under the same experimental conditions. The flowthrough containing the untagged protein was concentrated to 2.3 mg ml^{-1} in a 30 kDa cutoff ultrafiltration device (Millipore) with concomitant buffer exchange to storage buffer supplemented with 0.5 m*M* EDTA and 1 m*M* DTT.

2.2. Crystallization

Initial crystallization conditions were determined at 293 K with commercial sparse-matrix crystallization screens. Sitting-drop vapour-diffusion experiments were set up in 96-well CrystalQuick plates (Greiner Bio-One) using a Cartesian PixSys 4200 crystallization robot (Genomic Solutions) at the High Throughput Crystallization Laboratory (HTX Lab) of the EMBL Grenoble Outstation, Grenoble, France. The drops consisted of equal volumes (100 nl) of *Mh*GgH (at 9.5 mg ml^{-1} in 20 m*M* Tris–HCl, 400 m*M* NaCl) and crystallization solution and were equilibrated against 88 µl reservoir solution. Three-dimensional *Mh*GgH crystals appeared in condition No. 95 of the Morpheus sparse-matrix screen (Molecular Dimensions) after 1 d. The crystals were reproduced in-house using 24-well Cryschem M plates (Hampton Research) from drops composed of equal volumes (1 µl) of protein and precipitant solution equilibrated against 300 µl 0.1 *M* Tris–bicine pH 8.5, 0.1 *M* amino acids (glutamate, alanine, glycine, lysine and serine) and 24–34% GOL_P4K (glycerol, PEG 4000) as precipitant. Crystals were obtained after 1–2 d (Fig. 1*a*). SeMet-*Mh*GgH crystals were obtained using a drop ratio of 1:2 of protein solution (at 2.3 mg ml^{-1} in 20 m*M* Tris–HCl, 400 m*M* NaCl, 0.5 m*M* EDTA, 1 m*M* DTT) to precipitant equilibrated against a 300 µl reservoir of the crystallization condition identified for *Mh*GgH but with 24–28% GOL_P4K. Two SeMet-*Mh*GgH crystals were obtained after four months (Fig. 1*b*). Crystallization information is summarized in Table 2.

Table 2
Crystallization.

Method	Sitting-drop vapour diffusion
Plate type	96-well CrystalQuick plates (Greiner Bio-One) (screening); 24-well Cryschem M plates (Hampton Research) (production)
Temperature (K)	293
Protein concentration	*Mh*GgH, 9.5 mg ml^{-1}; SeMet-*Mh*GgH, 2.3 mg ml^{-1}
Buffer composition of protein solution	*Mh*GgH, 20 m*M* Tris–HCl pH 8.0, 400 m*M* NaCl; SeMet-*Mh*GgH, 20 m*M* Tris–HCl pH 8.0, 400 m*M* NaCl, 0.5 m*M* EDTA, 1 m*M* DTT
Composition of reservoir solution	0.1 *M* Tris–bicine pH 8.5, 0.1 *M* amino acids, 24–34% GOL_P4K
Volume and ratio of drop (protein:precipitant)	0.1 µl, 1:1 (*Mh*GgH screening); 2 µl, 1:1 (*Mh*GgH production); 3 µl, 1:2 (SeMet-*Mh*GgH)
Volume of reservoir	88 µl (screening); 300 µl (production)

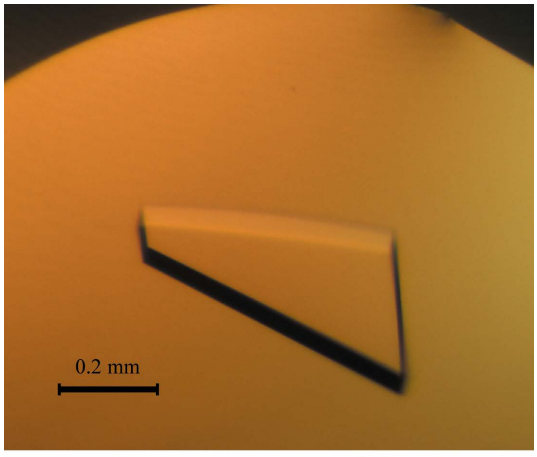

(*a*)

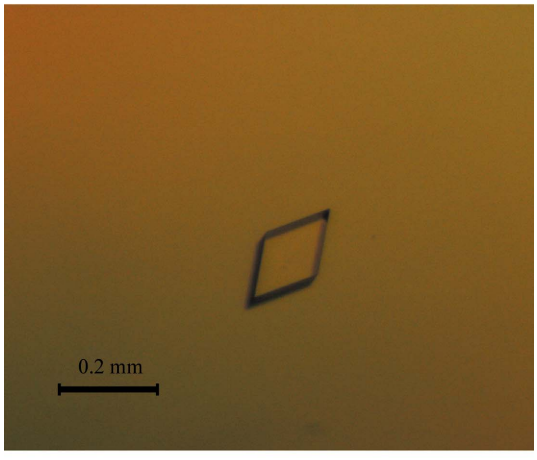

(*b*)

Figure 1
Crystals of *Mh*GgH (*a*) and SeMet-*Mh*GgH (*b*).

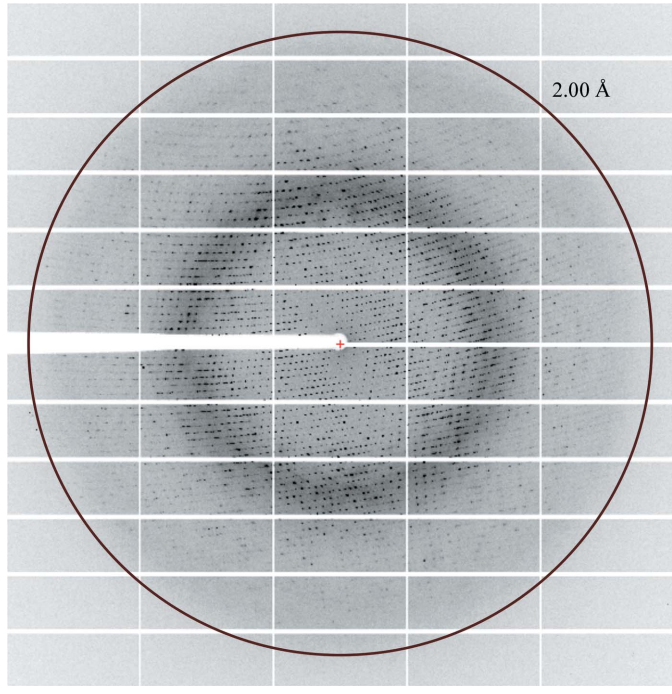

Figure 2
X-ray diffraction pattern from a SeMet-*Mh*GgH crystal. The circle corresponds to a resolution of 2.0 Å.

Table 3
Data collection and processing.

Values in parentheses are for the outer shell.

	Peak	Inflection point
Diffraction source	ID29, ESRF	
Wavelength (Å)	0.97909	0.97924
Temperature (K)	100	
Detector	PILATUS3 6M	
Crystal-to-detector distance (mm)	344.2	
Rotation range per image (°)	0.1	
Total rotation range (°)	150	
Exposure time per image (s)	0.02	
Space group	$P2_1$	
a, b, c (Å)	90.8, 86.1, 159.7	90.9, 86.3, 159.7
α, β, γ (°)	90.0, 93.0. 90.0	90.0, 93.0, 90.0
Mosaicity (°)	0.17	0.20
Resolution range (Å)	57.4–2.04 (2.07–2.04)	58.6–2.06 (2.09–2.06)
Total No. of reflections	428683	419987
No. of unique reflections	151619	148763
Completeness (%)	96.5 (82.1)	97.4 (87.6)
Multiplicity	2.8 (2.8)	2.8 (2.7)
Anomalous completeness (%)	68.3 (53.3)	85.0 (71.9)
Anomalous multiplicity	1.2 (1.7)	1.3 (1.5)
Half-set correlation $CC_{1/2}$	0.990 (0.659)	0.990 (0.657)
Half-set anomalous correlation CC_{anom}	0.355	0.166
$\langle I/\sigma(I)\rangle$	7.6 (1.6)†	7.1 (1.8)‡
$R_{r.i.m.}$	0.128 (0.776)	0.129 (0.690)
Overall B factor from Wilson plot (Å^2)	20.4	25.4

† $\langle I/\sigma(I)\rangle$ falls below 2.0 at 2.15 Å resolution. ‡ $\langle I/\sigma(I)\rangle$ falls below 2.0 at 2.09 Å resolution.

2.3. Data collection and processing

Diffraction data (Fig. 2) were collected from a single cryocooled (100 K) selenomethionine-containing *Mh*GgH crystal that had previously been cryoprotected with crystallization solution containing 30% GOL_P4K and flash-cooled in liquid nitrogen on beamline ID29 (de Sanctis *et al.*, 2012) of the European Synchrotron Radiation Facility (ESRF), Grenoble, France. Two data sets were collected at wavelengths of 0.97909 and 0.97924 Å, corresponding to the peak and the inflection point of the *K* absorption edge of selenium, respectively. The data sets were automatically processed by the *Grenoble Automatic Data procEssing* (*GrenADES*) pipeline (Monaco *et al.*, 2013) and scaled with *XSCALE* (Kabsch, 2010). X-ray diffraction data-collection and processing statistics are summarized in Table 3.

3. Results and discussion

Recombinant *Mh*GgH was expressed in *E. coli* and purified to homogeneity using a combination of immobilized metal-affinity and size-exclusion chromatography. The expressed construct encoded an N-terminal His tag, which was separated from the native *Mh*GgH sequence by a TEV protease recognition site that allowed proteolytic tag removal. TEV protease cleavage resulted in an additional Gly-Ala dipeptide N-terminal to the native *Mh*GgH amino-acid sequence (Table 1).

Initial crystallization conditions were identified using extensive sampling of commercial sparse-matrix crystallization screens at the EMBL Grenoble Outstation HTX Lab. The crystals were reproduced in-house, and optimized crystals obtained in 1–2 d diffracted X-rays to beyond 2.0 Å resolution at a synchrotron-radiation source. In order to solve the phase problem, selenomethionine-containing *Mh*GgH was produced. It was found that selenomethionine-labelled *Mh*GgH was considerably less soluble than the unlabelled protein under the same experimental conditions. Therefore,

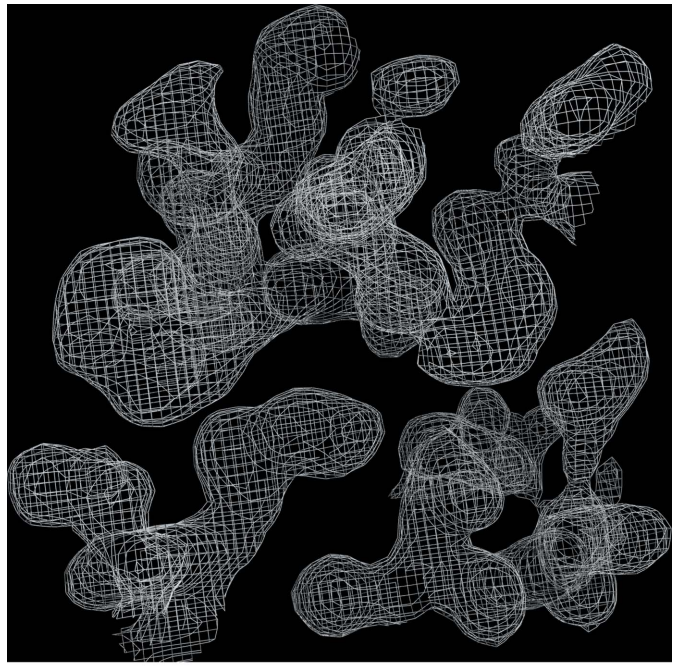

(*a*)

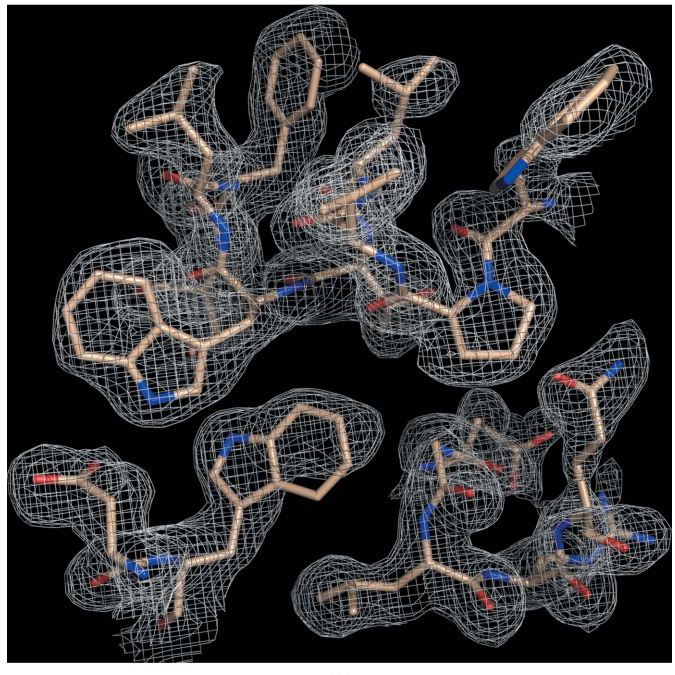

(*b*)

Figure 3
Experimental electron-density map for *Mh*GgH. (*a*) Solvent-flattened electron-density map (grey mesh) from *SHELXE* (Sheldrick, 2010). (*b*) Electron-density map as in (*a*) with superposed protein model (sticks) automatically built by *ARP*/*wARP* (Langer *et al.*, 2008).

selenomethionine-labelled *Mh*GgH could only be concentrated to a fourfold lower concentration than the unlabelled material. Under crystallization conditions similar to those for the wild-type protein, two SeMet-*Mh*GgH crystals were obtained after four months (Table 2). The slower crystallogenesis of selenomethionine-labelled *Mh*GgH is most likely to be owing to the lower sample concentration used in the crystallization assays.

The diffraction from a SeMet-*Mh*GgH crystal was measured on beamline ID29 at ESRF, Grenoble, France. The crystal belonged to the monoclinic space group $P2_1$ and diffracted to ∼2 Å resolution (Table 3). Analysis of the crystal content suggested the presence of four *Mh*GgH molecules in the asymmetric unit, corresponding to a Matthews coefficient of 3.07 Å^3 Da^{-1} and a solvent content of 59.9% (Winn *et al.*, 2011). Two diffraction data sets were recorded from a single crystal at wavelengths corresponding to the peak and the inflection point of the *K* absorption edge of selenium (Table 3). The phase problem was solved by two-wavelength anomalous diffraction phasing with the *SHELXC*/*SHELXD*/*SHELXE* pipeline (Sheldrick, 2010) and the *HKL2MAP* GUI (Pape & Schneider, 2004). *SHELXD* identified 27 of the 36 (nine per molecule) Se atoms present in the asymmetric unit (CC_{all} = 23.6%; CC_{weak} = 17.8%), corresponding to SeMet residues 153, 232, 246 and 432 of all molecules, as well as SeMet residue 28 of molecules *B* and *C*, SeMet residue 39 of molecules *A*, *B* and *C*, and SeMet residues 75 and 181 of molecules *A*, *B* and *D*. Experimental phasing with density modification using *SHELXE* resulted in excellent electron-density maps (Fig. 3), with a final FOM of 0.652 and a pseudo-free CC of 71.3%. The autotracing function of *SHELXE* produced a 1411-residue poly-Ala model (CC for partial structure against native data = 36.1%). Subsequent automated model building with *ARP*/*wARP* (Langer *et al.*, 2008) using the *SHELXE*-derived phases resulted in an initial model with 1677 (of 1792) residues built and sequenced. The *Mh*GgH crystallographic model was further improved through alternative cycles of manual building with *Coot* (Emsley *et al.*, 2010) and refinement with *PHENIX* (Adams *et al.*, 2010) and is currently in the last stages of refinement.

Acknowledgements

We acknowledge the ESRF for the provision of synchrotron-radiation facilities and thank the staff for help with data collection. Transnational Access to the High Throughput Crystallization Laboratory of the European Molecular Biology Laboratory Grenoble Outstation was supported by the European Community Seventh Framework Program (FP7/2007–2013) Grant Protein Production Platform (PCUBE Agreement No. 227764).

Funding information

The following funding is acknowledged: Fundação para a Ciência e a Tecnologia [studentship No. SFRH/BD/92955/2013 to Tatiana Barros Cereija; grant No. POCI-01-0145-FEDER-007274; grant No. UID/NEU/04539/2013 (POCI-01-0145-FEDER-007440); studentship No. SFRH/BPD/108299/2015 to Susana Alarico]; European Regional Development Fund (grant No. POCI-01-0145-FEDER-007274; grant No. UID/NEU/04539/2013; grant No. Norte-01-0145-FEDER-000012); COMPETE 2020 – Operational Programme for Competitiveness and Internationalization (POCI) (grant No. POCI-01-0145-FEDER-007274; grant No. UID/NEU/04539/2013); Norte Portugal Regional Operational Programme (NORTE 2020) (grant No. Norte-01-0145-FEDER-000012).

References

Adams, P. D. *et al.* (2010). *Acta Cryst.* D**66**, 213–221.
Alarico, S., Costa, M., Sousa, M. S., Maranha, A., Lourenço, E. C., Faria, T. Q., Ventura, M. R. & Empadinhas, N. (2014). *Sci. Rep.* **4**, 6766.
Behrends, V., Williams, K. J., Jenkins, V. A., Robertson, B. D. & Bundy, J. G. (2012). *J. Proteome Res.* **11**, 3888–3896.
Emsley, P., Lohkamp, B., Scott, W. G. & Cowtan, K. (2010). *Acta Cryst.* D**66**, 486–501.
Falkinham, J. O. (2010). *Future Microbiol.* **5**, 951–960.
Griffith, D. E. *et al.* (2007). *Am. J. Respir. Crit. Care Med.* **175**, 367–416.
Griffith, D. E., Brown-Elliott, B. A., Benwill, J. L. & Wallace, R. J. Jr (2015). *Annals ATS*, **12**, 436–439.
Henkle, E. & Winthrop, K. L. (2015). *Clin. Chest Med.* **36**, 91–99.
Kabsch, W. (2010). *Acta Cryst.* D**66**, 125–132.
Langer, G., Cohen, S. X., Lamzin, V. S. & Perrakis, A. (2008). *Nature Protoc.* **3**, 1171–1179.
Miyazaki, T., Ichikawa, M., Iino, H., Nishikawa, A. & Tonozuka, T. (2015). *J. Struct. Biol.* **190**, 21–30.
Monaco, S., Gordon, E., Bowler, M. W., Delagenière, S., Guijarro, M., Spruce, D., Svensson, O., McSweeney, S. M., McCarthy, A. A., Leonard, G. & Nanao, M. H. (2013). *J. Appl. Cryst.* **46**, 804–810.
Nessar, R., Cambau, E., Reyrat, J. M., Murray, A. & Gicquel, B. (2012). *J. Antimicrob. Chemother.* **67**, 810–818.
Nunes-Costa, D., Alarico, S., Dalcolmo, M. P., Correia-Neves, M. & Empadinhas, N. (2016). *Tuberculosis*, **96**, 107–119.
Nunes-Costa, D., Maranha, A., Costa, M., Alarico, S. & Empadinhas, N. (2017). *Glycobiology*, **27**, 213–227.
Pape, T. & Schneider, T. R. (2004). *J. Appl. Cryst.* **37**, 843–844.
Piersimoni, C. & Scarparo, C. (2008). *Lancet Infect. Dis.* **8**, 323–334.
Sanctis, D. de *et al.* (2012). *J. Synchrotron Rad.* **19**, 455–461.
Shahraki, A. H., Heidarieh, P., Bostanabad, S. Z., Khosravi, A. D., Hashemzadeh, M., Khandan, S., Biranvand, M., Schraufnagel, D. E. & Mirsaeidi, M. (2015). *Eur. J. Intern. Med.* **26**, 279–284.
Sheldrick, G. M. (2010). *Acta Cryst.* D**66**, 479–485.
Tiago, I., Maranha, A., Mendes, V., Alarico, S., Moynihan, P. J., Clarke, A. J., Macedo-Ribeiro, S., Pereira, P. J. & Empadinhas, N. (2012). *J. Bacteriol.* **194**, 7010–7011.
Winn, M. D. *et al.* (2011). *Acta Cryst.* D**67**, 235–242.